Available online at www.sciencedirect.com
ScienceDirect
Comput. Methods Appl. Mech. Engrg. 380 (2021) 113743
Computer methods in applied mechanics and engineering
www.elsevier.com/locate/cma

Unfitted Nitsche's method for computing band structures of phononic crystals with periodic inclusions

Hailong Guo[a], Xu Yang[b], Yi Zhu[c,d,*]

[a] School of Mathematics and Statistics, The University of Melbourne, Parkville, VIC 3010, Australia
[b] Department of Mathematics, University of California, Santa Barbara, CA, 93106, USA
[c] Yau Mathematical Sciences Center, Tsinghua University, Beijing 100084, China
[d] Yanqi Lake Beijing Institute of Mathematical Sciences and Applications, Beijing 101408, China

Received 11 August 2020; received in revised form 27 October 2020; accepted 20 February 2021
Available online 26 March 2021

Abstract

In this paper, we propose an unfitted Nitsche's method to compute the band structures of phononic crystal with periodic inclusions of general geometry. The proposed method does not require the background mesh to fit the interfaces of periodic inclusions, and thus avoids the expensive cost of generating body-fitted meshes and simplifies the inclusion of interface conditions in the formulation. The quasi-periodic boundary conditions are handled by the Floquet–Bloch transform, which converts the computation of band structures into an eigenvalue problem with periodic boundary conditions. More importantly, we show the well-posedness of the proposed method using a delicate argument based on the trace inequality, and further prove the convergence by the Babuška–Osborn theory. We achieve the optimal convergence rate at the presence of the periodic inclusions of general geometry. We demonstrate the theoretical results by two numerical examples, and show the capability of the proposed methods for computing the band structures without fitting the interfaces of periodic inclusions.

MSC: 78M10; 78A48; 47A70; 35P99

Keywords: Band structure; Phononic crystal; Unfitted mesh; High-contrast; Periodic inclusions

1. Introduction

Phononic crystals are synthetic materials with periodic structure. Similar to photonic crystals, they exhibit band-gap structures related to topological properties, which prevent elastic waves propagating in certain frequencies. This leads to a series of important applications such as ultrasound imaging and wireless communications. In literature, Economou and Sigalas [1] experimentally observed the band-gap in phononic crystals. Ammari et al. [2] mathematically proved the existence of band-gap in the high-contrast phononic crystal using the asymptotic expansion and the generalized Rouché's theorem. In general, phononic crystals with large band-gap is preferred due to the wide range of applications. One of the most influential accounts of band-gap optimization comes from Sigmund and Jensen who were one of the first to use topology optimization approach to design a phononic

* Corresponding author at: Yau Mathematical Sciences Center, Tsinghua University, Beijing 100084, China.
E-mail addresses: hailong.guo@unimelb.edu.au (H. Guo), xuyang@math.ucsb.edu (X. Yang), yizhu@tsinghua.edu.cn (Y. Zhu).

https://doi.org/10.1016/j.cma.2021.113743
0045-7825/

crystal with maximum relative band-gap size [3]. The main idea is to find the optimal arrangement of two different materials to achieve maximum band-gap. The geometric configuration of the two materials is continually updated during designing process. The main computational challenge is the numerical solution of heterogeneous eigenvalue problems with the moving material interface.

Another desire was brought about by the recent increasing interest in wave propagation in topological phononic materials. One of the key problems is to understand the band structure of bulk phononic crystals [4]. In generic cases, it is hard to obtain the explicit form of band structures with complete analytical techniques, and thus numerical computation plays an essential role. Early works on numerical approximations can be traced back to [5] where Kushwaha et al. used the plane-wave expansion to compute the band structure. The transfer matrix method was also adopted by Sigalas and Soukoulis [6] to simulate the propagation of elastic waves through disordered solid. To date, various methods have been developed to compute the band structure of phononic crystals including the multiple scattering method [7], the finite difference time domain method [8], the meshless method [9], the (multiscale) finite element method [10–13], the homogenization method [14–16], and the singular boundary method [17].

Among the aforementioned methods, the numerical difficulties come from two different perspectives: one is the heterogeneous primitive cell of the phononic crystals and the other is how to efficiently impose the quasi-periodic boundary condition. Although extensive research has been carried out on the computing bandgap of phononic crystal, very few has addressed the complication brought by adjusting material interfaces for instance in the material design. Until recently, Wang et al. [18] proposed a Petrov–Galerkin immersed finite element method to compute the band structure of the phononic crystal and imposed the quasi-periodic boundary condition directly. However, the rigorous analysis of unfitted numerical methods is still lacking in the literature.

In this paper, we propose an unfitted Nitsche's method to compute the band structures of phononic crystal with periodic inclusions of general geometry, and prove the convergence with rigorous mathematical analysis. The heterogeneous primitive cell of the phononic crystal is described by the interface condition which we can build into a variational framework with the help of the Floquet–Bloch theory. To handle the quasi-periodic boundary condition, the Floquet–Bloch transform is applied which reformulates the model equation with quasi-periodic boundary conditions into an equivalent model equation with periodic boundary conditions and Bloch-type interface condition. Then, the reformulated model equations can be numerically tackled by the unfitted Nitsche's type method [19–23] using uniform meshes. The proposed unfitted finite element method is motivated by our previous work of computing edge modes in topological materials [24]. The first advantage is that it uses meshes independent of the location of the material interfaces. It reduces the computational cost of generating body-fitted meshes, especially in designing phononic crystals. The second advantage is that it is straightforward to impose the periodic boundary conditions since only uniform meshes are used. Remark that imposing periodic boundary conditions on general unstructured meshes is quite technically involved, and interesting readers are referred to [25,26] and the references therein about the recent development of imposing periodic boundary condition on general unstructured meshes.

As mentioned in our previous work [24], the discrete Nitsche's bilinear form involves the solution itself in addition to its gradient which cause the difficulties in the analysis. In this paper, we establish a solid theoretical analysis for the proposed unfitted finite element methods by conquering the above difficulties. Specifically, we show the discrete equation is well defined by using a delicate trace inequality on the cut element, the Poincaré inequality between the energy norm of the original model equation and the energy norm of the modified model equation, and the explicit relation between the strain tensor and stress tensor. By the aid of the Babuška–Osborn spectral approximation theory [27,28], the proposed unfitted finite element method is proven to have the optimal approximation property for the eigenvalues and eigenfunctions in the high-contrast heterogeneous primitive cell.

The paper is organized as follows. In Section 2, we introduce the model of plane-wave propagation in the phononic crystals. In Section 3, we propose the unfitted numerical method to compute the band structure of phononic crystal based on the Bloch–Floquet theory and prove the proposed method admits a unique solution. In Section 4, we carry out the optimal error analysis. In Section 5, we present some numerical examples in a realistic setting to verify and validate our theoretical discoveries. At the end, some conclusion is drawn in Section 6.

2. Model of phononic crystal

In this section, we first present a little digest to the two-dimensional phononic crystal. Then we consider the model of in-plane wave propagation.

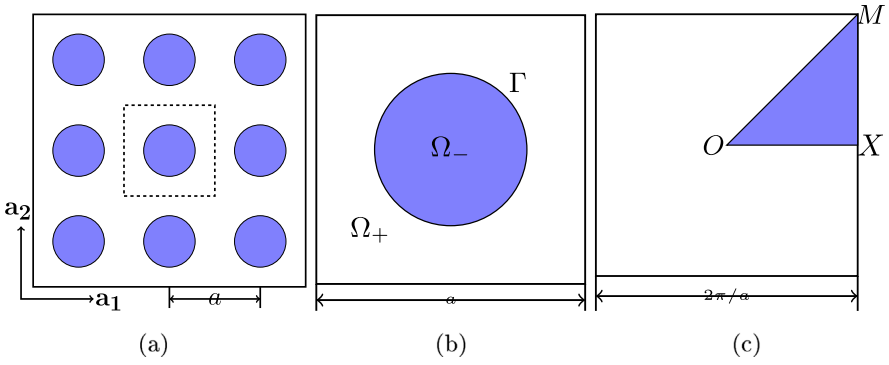

Fig. 1. Bravais lattice Γ. (a) 2D square lattice; (b) the primitive cell; (c) the first Brillouin zone.

2.1. Problem setup

Phononic crystal is designed from periodically arrangement of two different materials to achieve extraordinary properties like negative refractive index. The body of phononic crystal is a kind of high-contrast materials with heterogeneous primitive cells.

We will mainly focus phononic crystals with two-dimensional Bravais lattice Λ formed by two primitive vectors $\boldsymbol{a}_1$ and $\boldsymbol{a}_2$, i.e.

$$\Lambda = \mathbb{Z}\boldsymbol{a}_1 + \mathbb{Z}\boldsymbol{a_2} = \{m_1\boldsymbol{a}_1 + m_2\boldsymbol{a}_2 : \ m_1, m_2 \in \mathbb{Z}\}. \tag{2.1}$$

An example of square lattice with $\boldsymbol{a}_1 = (a, 0)^T$ and $\boldsymbol{a}_2 = (0, a)^T$ is shown in Fig. 1a. The primitive cell (or fundamental domain) Ω of Bravais lattice Λ is defined as

$$\Omega = \{\theta_1\boldsymbol{a}_1 + \theta_2\boldsymbol{a}_2 : 0 \le \theta_1, \theta_2 \le 1\}, \tag{2.2}$$

which is illustrated in Fig. 1b for the square lattice.

Denote the generating basis of the reciprocal lattice (or dual lattice) by $\boldsymbol{k}_i$ for $i = 1, 2$, which satisfy

$$\boldsymbol{k}_i \cdot \boldsymbol{a}_j = 2\pi\delta_{i,j}, \quad \forall i, j = 1, 2, \tag{2.3}$$

where δ_{ij} is the Kronecker delta. Then, the reciprocal lattice Λ^* is

$$\Lambda^* = \mathbb{Z}\boldsymbol{k}_1 + \mathbb{Z}\boldsymbol{k_2} = \{m_1\boldsymbol{k}_1 + m_2\boldsymbol{k}_2 : \ m_1, m_2 \in \mathbb{Z}\}. \tag{2.4}$$

The fundamental domain of the reciprocal lattice is

$$\Omega^* = \{\theta_1\boldsymbol{k}_1 + \theta_2\mathbf{k}_2 : 0 \le \theta_1, \theta_2 \le 1\}, \tag{2.5}$$

which is termed as the first Brillouin zone [29]. Again, we illustrate the first Brillouin zone for the square lattice in Fig. 1c, where the triangle formed by the point O, X, and M is referred as the irreducible Brillouin zone [29].

The primitive cell Ω of the phononic crystal involves hard inclusion of one material Ω_- into a background material Ω_+. The background material is referred as the matrix and the inclusion is also referred as fiber. The matrix Ω_+ and the inclusion Ω_- are separated by the material interface Γ. In Fig. 1b, we show the fundament cell with a circular inclusion.

In this paper, we assume that both the inclusions and matrix are homogeneous isotropic elastic solids. We use λ^+ (or λ^-) denote the first Lamé parameter of matrix (or inclusion) and μ^+ (or μ^-) denote the second Lamé parameter of matrix (or inclusion). Similarly, let ρ^+ and ρ^- denote the mass density of the matrix and inclusion, respectively. To simplify the notation, we let

$$\lambda = \begin{cases} \lambda^-, & \text{in } \Omega^-, \\ \lambda^+, & \text{in } \Omega^+, \end{cases} \quad \mu = \begin{cases} \mu^-, & \text{in } \Omega^-, \\ \mu^+, & \text{in } \Omega^+, \end{cases} \quad \text{and } \rho = \begin{cases} \rho^-, & \text{in } \Omega^-, \\ \rho^+, & \text{in } \Omega^+. \end{cases} \tag{2.6}$$

For any vector-valued function $\boldsymbol{v}$ defined on Ω, let $[\![\boldsymbol{v}]\!]$ be the jump of function $\boldsymbol{v}$ crossing the interface Γ, i.e.

$$[\![\boldsymbol{v}]\!](\boldsymbol{x}) = \boldsymbol{v}|_{\Omega^+}(\boldsymbol{x}) - \boldsymbol{v}|_{\Omega^-}(\boldsymbol{x}) \tag{2.7}$$

where $\boldsymbol{x} \in \Gamma$.

Throughout the paper, the standard notations for (complex-valued) Sobolev spaces and their associated norms are used as in [30–32]. Given a bounded subdomain $D \subset \Omega$ and any positive integer k, the Sobolev space with norm $\|\cdot\|_{k,D}$ and seminorm $|\cdot|_{k,D}$ is denoted by $H^k(D)$. When $k = 0$, $H^k(D)$ reduces to the standard $L^2(D)$ space. Let $(\cdot,\cdot)_D$ denote the standard inner products of $L^2(D)$. When $D = \Omega$, the subscript is omitted. For a bounded domain $D = D^+ \cup D^-$ with $D^+ \cap D^- = \emptyset$, let $H^k(D^+ \cup D^-)$ be the function space consisting of piecewise Sobolev functions w such that $w|_{D^+} \in H^k(D^+)$ and $w|_{D^-} \in H^k(D^-)$, whose norm is defined as

$$\|w\|_{k,D^+\cup D^-} = \left(\|w\|^p_{k,D^+} + \|w\|^p_{k,D^-}\right)^{1/p}, \tag{2.8}$$

and seminorm is defined as

$$|w|_{k,p,D^+\cup D^-} = \left(|w|^p_{k,D^+} + |w|^p_{k,D^-}\right)^{1/p}. \tag{2.9}$$

To avoid abuse of notation, the same notation is applied to the vector-valued function $\boldsymbol{w} = (w_1, w_2)^T$.

For any vectors $\boldsymbol{v}$ and $\boldsymbol{w}$, let $\boldsymbol{v} \otimes \boldsymbol{w}$ be the tensor product of $\boldsymbol{v}$ and $\boldsymbol{w}$ and let $\boldsymbol{v} \odot \boldsymbol{w} = \frac{1}{2}(\boldsymbol{v} \otimes \boldsymbol{w} + \boldsymbol{w} \otimes \boldsymbol{v})$ be the symmetric tensor product. For the quasi-momentum $\boldsymbol{k}$ in the Brillouin zone, define the shift differential operator $\nabla_{\boldsymbol{k}}$ as

$$\nabla_{\boldsymbol{k}} = \nabla + \mathrm{i}\boldsymbol{k}, \tag{2.10}$$

where i is the imaginary unit.

In this paper, we use the constant C, with or without a subscript, to denote a generic positive constant which can be different at different occurrences. In addition, it is independent of mesh size and the location of the interface. By $x \lesssim y$, we mean that there exists a constant C such that $x \le Cy$.

Before ending this section, we introduce some additional function spaces for Bloch-periodic (or quasi-periodic) functions

$$H^k_{per}(\Omega) = \left\{\boldsymbol{w}(\boldsymbol{x}) \in H^k(\Omega) : \boldsymbol{w}(\boldsymbol{x} \pm \boldsymbol{a}_j) = \boldsymbol{w}(\boldsymbol{x}) \text{ on } \partial\Omega \text{ and } j = 1, 2\right\}, \tag{2.11}$$

$$H^k_{\boldsymbol{k}}(\Omega) = \left\{\boldsymbol{w}(\boldsymbol{x}) : \exp(-\mathrm{i}\boldsymbol{k}\cdot\boldsymbol{x})\boldsymbol{w}(\boldsymbol{x}) \in H^k_{per}(\Omega)\right\}. \tag{2.12}$$

It is worth noting that the Sobolev space $H^k_{per}(\Omega)$ and $H^k_{\boldsymbol{k}}(\Omega)$ are both complex-valued.

2.2. In-plane wave propagation

The in-plane wave propagation is modeled by the elastodynamics operator

$$\mathcal{L}\boldsymbol{\phi} = -\nabla\cdot\boldsymbol{\sigma}[\boldsymbol{\phi}] = -\nabla\cdot\mathbf{C}\boldsymbol{\epsilon}[\boldsymbol{\phi}]. \tag{2.13}$$

where $\boldsymbol{\phi} = (\phi_1, \phi_2)^T$ is the displacement vector and $\mathbf{C}$ is the fourth-order stiffness tensor. In (2.13), $\boldsymbol{\epsilon}$ is the strain tensor which is related to the displacement via

$$\boldsymbol{\epsilon}[\boldsymbol{\phi}] = \nabla \odot \boldsymbol{\phi}, \tag{2.14}$$

and $\boldsymbol{\sigma}$ is the stress tensor. For the homogeneous isotropic material, the stress tensor and strain tensor are related by the Hook's law, i.e.

$$\boldsymbol{\sigma}[\boldsymbol{\phi}] = \mathbf{C}\boldsymbol{\epsilon}[\boldsymbol{\phi}] = 2\mu\boldsymbol{\epsilon}[\boldsymbol{\phi}] + \lambda\mathrm{tr}(\boldsymbol{\epsilon}[\boldsymbol{\phi}])\mathbb{I}_2. \tag{2.15}$$

where $\mathrm{tr}(A)$ is the trace of the matrix A and $\mathbb{I}_2$ is the 2×2 identity matrix.

Let $\boldsymbol{k} \in \Omega^*$ be the quasi-momentum. According to the Bloch theory [29], the in-plane wave propagation in phononic crystal can be reformulated to solve the following quasi-periodic eigenvalue problem [14,16]: find $(\omega^2, \boldsymbol{\phi}) \in \mathbb{R} \times H^1_{\boldsymbol{k}}(\Omega)$ such that

$$\begin{cases} \mathcal{L}\boldsymbol{\phi} = \omega^2\rho\boldsymbol{\phi}, & \text{in } \Omega \setminus \Gamma, \\ [\![\boldsymbol{\phi}]\!] = [\![\mathbf{C}(\nabla \odot \boldsymbol{\phi})\boldsymbol{n}]\!] = 0, & \text{on } \Gamma, \end{cases} \tag{2.16}$$

where $\boldsymbol{n}$ is the unit normal vector of Γ pointing from Ω^- to Ω^+.

For any fixed $\boldsymbol{k} \in \Omega^*$, the eigenvalue problems (2.16) admits a sequence of eigenvalues $0 \leq \omega^2_{\boldsymbol{k},1} \leq \omega^2_{\boldsymbol{k},2} \leq \omega^2_{\boldsymbol{k},3} \leq \cdots \to \infty$ and corresponding eigenfunctions $\boldsymbol{\phi}_{\boldsymbol{k},1}, \boldsymbol{\phi}_{\boldsymbol{k},2}, \boldsymbol{\phi}_{\boldsymbol{k},3}, \ldots$ which are orthogonal in a ρ-weighted $L^2_{\boldsymbol{k}}(\Omega)$, i.e. $(\rho\boldsymbol{\phi}_{\boldsymbol{k},j}, \boldsymbol{\phi}_{\boldsymbol{k},k}) = \delta_{jk}$. As $\boldsymbol{k}$ varies in Ω^*, each eigenvalue $\omega^2_{\boldsymbol{k},n}$ forms a Lipschitz continuous function [33] referred to as a dispersion band function. Thus the whole spectrum exhibits a band structure with or without gaps between two adjacent bands.

In general, the eigenvalues can not be obtained analytically. Thus the band structures can not be represented in an explicit way. Only in certain asymptotic regimes, low-lying eigenvalues of (2.16) can be constructed with delicate asymptotic techniques. For instance, Ammari et al. [2] obtained the asymptotic expansions of the band functions in subwavelength limit of high contrast phononic crystals, and further proved the existence of the band gaps in this limit. The band structures in generic setups can only rely on numerical computations. We remark that $\omega^2_{\boldsymbol{k},n} = 0$ if and only if $n = 1$ and $\boldsymbol{k} = 0$, see for instance [34] and reference therein. In this case, the corresponding eigenfunction is constant, i.e., $\boldsymbol{\phi}_{\boldsymbol{0},1} = 1$. In the rest of this paper, we shall exclude this exceptional case. In addition, due to periodicity and symmetry, we only need to consider the case that the quasi-momentum $\boldsymbol{k}$ belongs to the irreducible Brillouin zone.

3. Unfitted Nitsche's method for computing band structure

In this section, we are going to propose an unfitted numerical method to efficiently compute band structures for generic phononic crystals. The numerical challenges brought by the eigenvalue problem (2.16) is twofold: one is quasi-periodic nature of the Bloch wave and the other one is the inhomogeneity of the material. These challenges shall be discussed in the following subsections.

3.1. Bloch–Floquet theory

To address the first numerical challenge, we apply the Bloch–Floquet transform $\boldsymbol{\phi}(\boldsymbol{x}) = e^{\mathrm{i}\boldsymbol{k}\cdot\boldsymbol{x}}\boldsymbol{u}(\boldsymbol{x})$. The quasi-periodic eigenvalue problem can be reformulated as: find $(\omega^2, \boldsymbol{u}) \in \mathbb{R} \times H^1_{per}(\Omega)$ such that

$$\begin{cases} \mathcal{L}_{\boldsymbol{k}}\boldsymbol{u} = \omega^2\rho\boldsymbol{u}, & \text{in } \Omega \setminus \Gamma, \\ [\![\boldsymbol{u}]\!] = [\![\mathbf{C}(\nabla_{\boldsymbol{k}} \odot \boldsymbol{u})\boldsymbol{n}]\!] = 0, & \text{on } \Gamma, \end{cases} \tag{3.1}$$

where the differential operator $\mathcal{L}_{\boldsymbol{k}}$ is defined as

$$\mathcal{L}_{\boldsymbol{k}}\boldsymbol{u} = \nabla_{\boldsymbol{k}} \cdot \mathbf{C}(\nabla_{\boldsymbol{k}} \odot \boldsymbol{u}), \tag{3.2}$$

with $\nabla_{\boldsymbol{k}}$ being the shift differential operator defined in (2.10). We want to remark that

$$\mathbf{C}(\nabla_{\boldsymbol{k}} \odot \boldsymbol{u}) = 2\mu\nabla_{\boldsymbol{k}} \odot \boldsymbol{u} + \lambda(\nabla_{\boldsymbol{k}} \cdot \boldsymbol{u})\mathbb{I}_2 \tag{3.3}$$

is termed as the modified stress tensor.

For any quasi-momentum $\boldsymbol{k}$, it is not difficult to see that $\mathcal{L}_{\boldsymbol{k}}$ is a self-adjoint positive definite operator. The spectrum of the elastodynamics operator $\mathcal{L}$ is the union of spectrum of $\mathcal{L}_{\boldsymbol{k}}$ for all $\boldsymbol{k} \in \Omega^*$. Notice that the Bloch–Floquet transform $\phi(\boldsymbol{x}) = e^{\mathrm{i}\boldsymbol{k}\cdot\boldsymbol{x}}\boldsymbol{u}(\boldsymbol{x})$ is an isomorphism from $H^1_{\boldsymbol{k}}(\Omega)$ to $H^1_{per}(\Omega)$. Then, we have the following Poincaré inequality:

$$C_0[(\mathbf{C}(\nabla \odot \boldsymbol{u}), \nabla \odot \boldsymbol{u}) + (\mathbf{C}(\boldsymbol{k} \odot \boldsymbol{u}), \boldsymbol{k} \odot \boldsymbol{u})] \leq (\mathbf{C}(\nabla_{\boldsymbol{k}} \odot \boldsymbol{u}), \nabla_{\boldsymbol{k}} \odot \boldsymbol{u}), \tag{3.4}$$

where C_0 is a positive constant.

3.2. Formulation of the unfitted Nitsche's method

To find the band structure of $\mathcal{L}$, it suffices to solve a series of periodic eigenvalue problem (3.1). The main numerical barrier is how to efficiently handle the interface condition. We alleviate this barrier by introducing a new unfitted Nitsche's method which is seamlessly infusing with the Bloch–Floquet theory.

One merit of unfitted Nitsche's method is to use meshes independent of the location of the material interface. Due to the lattice structure of the phononic crystal, uniform meshes are adopted. To show the main idea, we use the square lattice as the prototype model but the method works for other lattices. We generate a uniform mesh $\mathcal{T}_h$

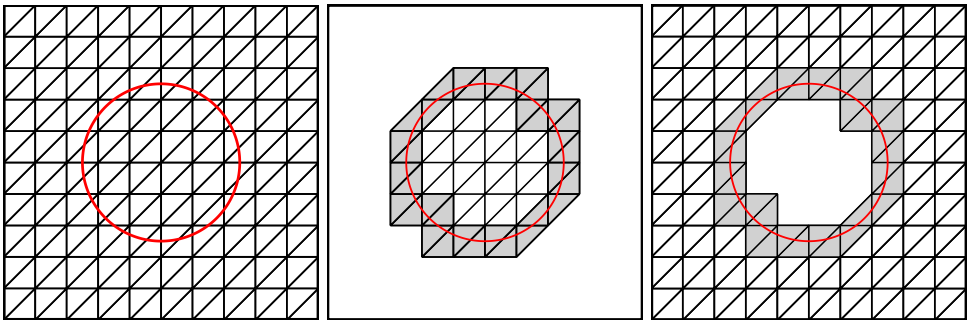

Fig. 2. Illustration of the overlapping domain decomposition of Ω (a) Unfitted meshes on Ω; (b) Subdomain Ω_h^-; (c) Subdomain Ω_h^+.

on the fundamental domain Ω of the square lattice by partitioning it into N^2 subsquares with mesh size $h = \frac{a}{N}$ and then splitting each subsquare into isosceles right triangles, see Fig. 2a.

To handle the non-smoothness of the Bloch wave across the material interface, we decompose the fundamental domain Ω into two overlapping subdomains Ω_h^+ and Ω_h^- as

$$\Omega_h^+ = \cup\{K \in \mathcal{T}_h : K \cap \Omega^+ \neq \emptyset\}, \quad \text{and} \quad \Omega_h^- = \cup\{K \in \mathcal{T}_h : K \cap \Omega^- \neq \emptyset\}. \tag{3.5}$$

We illustrate the decomposition in Fig. 2. It is undeniable that intersection of Ω_h^+ and Ω_h^- is nonempty. In that sense, $\Omega_h^\pm$ are termed as fictitious domains. Similarly, we can define two subtriangulations $\mathcal{T}_h^+$ and $\mathcal{T}_h^-$ as

$$\mathcal{T}_h^+ = \{K \in \mathcal{T}_h : K \subset \Omega_h^+\}, \quad \text{and} \quad \mathcal{T}_h^- = \{K \in \mathcal{T}_h : K \subset \Omega_h^-\}. \tag{3.6}$$

The common subsets of $\mathcal{T}_h^+$ and $\mathcal{T}_h^-$ is denoted by $\mathcal{T}_{\Gamma,h}$ which denotes the set of interface elements.

Based on the overlapping domain decomposition, we can define the finite element space on each of them independently. To do this, let V_h^s $(s = \pm)$ be the standard continuous linear finite element space on Ω_h^s, i.e.,

$$V_h^s = \left\{ \boldsymbol{v}_h \in \left[C^0(\Omega_h^s)\right]^2 : \boldsymbol{v}|_K \in [\mathbb{P}_1(K)]^2 \text{ for any } K \in \mathcal{T}_h^s \right\}, \tag{3.7}$$

with $\mathbb{P}_k(K)$ being the space of polynomials of degree k on the element K.

Then the finite element space for the unfitted Nitsche's method is defined as $V_h = V_h^+ \times V_h^-$, i.e.,

$$V_h = \left\{ \boldsymbol{v}_h = (\boldsymbol{v}_h^+, v_h^-) : \boldsymbol{v}_h^s \in V_h^s,\ s = \pm \right\}. \tag{3.8}$$

To impose the periodic boundary condition, we introduce $V_{h,per}$ as a subspace of V_h which is defined as

$$V_{h,per} = \left\{ \boldsymbol{v}_h \in V_h : \boldsymbol{v}_h(\boldsymbol{x} \pm \boldsymbol{a}_j) = \boldsymbol{v}_h(\boldsymbol{x}) \text{ on } \partial\Omega \text{ and } j = 1, 2 \right\}. \tag{3.9}$$

Note that for any interface element $K \in \mathcal{T}_{\Gamma,h}$, there are two sets of vector-valued basis functions for any element K-one for V_h^+ and the other for V_h^-.

For any interface element $K \in \mathcal{T}_{\Gamma,h}$, let $K^\pm$ denote the part of the triangle inside $\Omega^\pm$ and $|K^\pm|$ denote the area of $K^\pm$. Similarly, let $\Gamma_K = \Gamma \cap K$ be the part of Γ in the element K and let $|\Gamma_K|$ be the length of Γ_K. Before defining the weak formulation, it is necessary to introduce some parameters. For $s = \pm$, let $\beta^s = 2\mu^s + \lambda^s$. Define two weights as [35]

$$\kappa^+ = \frac{\beta^-}{\beta^+ + \beta^-}, \quad \kappa^- = \frac{\beta^+}{\beta^+ + \beta^-}, \tag{3.10}$$

which satisfy $\kappa^+ + \kappa^- = 1$. Based on the two weights, we can define a weighted averaging of the displacement vector on the interface Γ as

$$\{\{\boldsymbol{u}\}\} = \kappa^+ \boldsymbol{u}^+ + \kappa^- \boldsymbol{u}^-. \tag{3.11}$$

Also, we define the parameter for the weak formulation

$$\gamma = \hat{\gamma}\frac{\beta^+\beta^-}{\beta^+ + \beta^-} \tag{3.12}$$

where $\hat{\gamma}$ is a sufficiently large constant called the stabilizing parameter.

Define the Nitsche's sesquilinear form $a_h(\cdot,\cdot) : H^1_{per}(\Omega) \times H^1_{per}(\Omega) \to \mathbb{R}$ as

$$\begin{aligned} a_h(\boldsymbol{u}_h, \boldsymbol{v}_h) = &\sum_{s=\pm}\int_{\Omega^s} \mathbf{C}(\nabla_{\boldsymbol{k}} \odot \boldsymbol{u}_h) : (\overline{\nabla_{\boldsymbol{k}} \odot \boldsymbol{v}_h})d\boldsymbol{x} \\ &+ \int_\Gamma \{\{\mathbf{C}\,(\nabla_{\boldsymbol{k}} \odot \boldsymbol{u}_h)\,\boldsymbol{n}\}\} \cdot [\![\overline{\boldsymbol{v}_h}]\!] ds \\ &+ \int_\Gamma [\![\boldsymbol{u}_h]\!] \cdot \{\{\overline{\mathbf{C}\,(\nabla_{\boldsymbol{k}} \odot \boldsymbol{u}_h)\,\boldsymbol{n}}\}\} ds \\ &+ \frac{\gamma}{h}\int_\Gamma [\![\boldsymbol{u}_h]\!] \cdot [\![\overline{\boldsymbol{v}_h}]\!] ds, \end{aligned} \tag{3.13}$$

where h is the mesh size, $\mathbf{C}$ is the fourth-order stiffness tensor, and $A : B$ is the Frobenius inner product of two matrices A and B.

Given a quasi-momentum $\boldsymbol{k}$ in the reduced Brillouin zone, the unfitted Nitsche's method for the eigenvalue problem (3.1) is to find the eigenpair $(\omega_h^2, \boldsymbol{u}_h) \in \mathbb{R} \times V_{h,per}$ such that

$$a_h(\boldsymbol{u}_h, \boldsymbol{v}_h) = \omega_h^2 b(\boldsymbol{u}_h, \boldsymbol{v}_h), \quad \forall\, \boldsymbol{v}_h \in V_{h,per}, \tag{3.14}$$

where

$$b(\boldsymbol{u}_h, \boldsymbol{v}_h) = \int_\Omega \rho \boldsymbol{u}_h \overline{\boldsymbol{v}_h} d\boldsymbol{x}. \tag{3.15}$$

Remark 3.1. Using the definition of the fourth-order stiffness tensor $\mathbf{C}$, we can write the Nitsche's sesquilinear form $a_h(\cdot,\cdot)$ into the following equivalent form

$$\begin{aligned} &a_h(\boldsymbol{u}_h, \boldsymbol{v}_h) \\ =&2\mu\sum_{s=\pm}\int_{\Omega^s} (\nabla_{\boldsymbol{k}} \odot \boldsymbol{u}_h) : (\overline{\nabla_{\boldsymbol{k}} \odot \boldsymbol{v}_h})d\boldsymbol{x} + \lambda\sum_{s=\pm}\int_{\Omega^s} (\nabla_{\boldsymbol{k}} \cdot \boldsymbol{u}_h)(\overline{\nabla_{\boldsymbol{k}} \cdot \boldsymbol{v}_h})d\boldsymbol{x} \\ &+ \int_\Gamma \{\{2\mu(\nabla_{\boldsymbol{k}} \odot \boldsymbol{u}_h)\boldsymbol{n} + \lambda(\nabla_{\boldsymbol{k}} \cdot \boldsymbol{u}_h)\boldsymbol{n}\}\} \cdot [\![\overline{\boldsymbol{v}_h}]\!] ds \\ &+ \int_\Gamma [\![\boldsymbol{u}_h]\!] \cdot \{\{\overline{2\mu(\nabla_{\boldsymbol{k}} \odot \boldsymbol{v}_h)\boldsymbol{n} + \lambda(\nabla_{\boldsymbol{k}} \cdot \boldsymbol{v}_h)\boldsymbol{n}}\}\} ds \\ &+ \frac{\gamma}{h}\int_\Gamma [\![\boldsymbol{u}_h]\!] \cdot [\![\overline{\boldsymbol{v}_h}]\!] ds. \end{aligned} \tag{3.16}$$

From this equivalent expression, it is not difficult to see that $a_h(\cdot,\cdot)$ is a symmetric sesquilinear form and the eigenvalues ω_h^2 are real.

Remark 3.2. To make the method be more robust with respect to small element cut, we can adopt the ghost penalty technique [36] to add more stabilizing terms in the vicinity of cut element.

Remark 3.3. The integral on the interface can be approximated by higher-order quadrature developed in the literature such as the method of moment-fitting [37], so that the quadrature approximation will not affect the overall discretization error. For the sake of easing presentation, we shall not consider the quadrature error in the overall estimate.

3.3. Well-posedness of unfitted Nitsche's method

This subsection is devoted to establishing the well-posedness of the proposed unfitted Nitsche's method (3.14). We start with showing the following consistency results:

Theorem 3.1. *Let $(\omega^2, \boldsymbol{u})$ be the eigenpair of the eigenvalue problem (3.1). Then, we have*

$$a_h(\boldsymbol{u}, \boldsymbol{v}) = \omega^2 b_h(\boldsymbol{v}, \boldsymbol{u}), \quad \forall\, \boldsymbol{v} \in H^1_{per}(\Omega). \tag{3.17}$$

Proof. The exact solution $\boldsymbol{u}$ satisfies $[\![\boldsymbol{u}]\!] = [\![\mathbf{C}\,(\nabla_{\boldsymbol{k}} \odot \boldsymbol{u})\,\boldsymbol{n}]\!] = 0$, on Γ. Using this fact and the Green's formulation, We can derive the Nitsche's weak formulation via the same technique as Nitsche's method for general boundary conditions as in [38]. □

Let us introduce the following interface boundary value problem in $H^1_{per}(\Omega)$

$$\begin{cases} \mathcal{L}_{\boldsymbol{k}} \boldsymbol{w} = \boldsymbol{f}, & \text{in } \Omega \setminus \Gamma, \\ [\![\boldsymbol{w}]\!] = [\![\mathbf{C}(\nabla_{\boldsymbol{k}} \odot \boldsymbol{w})\boldsymbol{n}]\!] = 0, & \text{on } \Gamma. \end{cases} \tag{3.18}$$

Furthermore, let w_h be its finite element solution by the unfitted Nitsche's finite element method. Taking $\boldsymbol{v}_h$ as any function in the unfitted Nitsche's finite element space $V_{h,per}$ in (3.17), it is straightforward to verify that

$$a_h(\boldsymbol{w} - \boldsymbol{w}_h, \boldsymbol{v}_h) = 0, \quad \forall \boldsymbol{v}_h \in V_{h,per}, \tag{3.19}$$

which is termed as the Galerkin orthogonality.

We are now in a position to show the stability of the unfitted Nitsche's method. Before that, we need to introduce some norms. For any quasi-momentum $\boldsymbol{k}$ in the reduced Brillouin zone, we introduce the following norm

$$\begin{aligned} |\!|\!| \boldsymbol{v}_h |\!|\!|^2 = & \sum_{s=\pm} \left(\mathbf{C}\,(\nabla_{\boldsymbol{k}} \odot \boldsymbol{v}_h)\,,\, \nabla_{\boldsymbol{k}} \odot \boldsymbol{v}_h\right)_{\Omega^s} \\ & + \sum_{K \in \mathcal{T}_{\Gamma,h}} h \| \{\!\{\mathbf{C}(\nabla_{\boldsymbol{k}} \odot \boldsymbol{v}_h)\boldsymbol{n}\}\!\} \|^2_{0,\Gamma_K} \\ & + \sum_{K \in \mathcal{T}_{\Gamma,h}} \frac{\gamma}{h} \| [\![\boldsymbol{v}_h]\!] \|^2_{0,\Gamma_K}. \end{aligned} \tag{3.20}$$

To show the well-posedness of the unfitted Nitsche's method, we need several technical lemmas. We begin with the trace inequality.

Lemma 3.2. *Let $\boldsymbol{v}_h$ be a finite element function in $V_{per,h}$ and $\boldsymbol{k}$ be a quasi-momentum in the reduced Brillouin zone. Then, the following inequalities hold:*

$$\| \{\!\{\mathbf{C}(\boldsymbol{k} \odot \boldsymbol{v}_h)\boldsymbol{n}\}\!\} \|^2_{0,\Gamma_K} \le C_1 h^{-1} \| \mathbf{C}(\boldsymbol{k} \odot \boldsymbol{v}_h) \|^2_{0,K^+ \cup K^-}, \tag{3.21}$$

$$\| \{\!\{\mathbf{C}(\nabla \odot \boldsymbol{v}_h)\boldsymbol{n}\}\!\} \|^2_{0,\Gamma_K} \le C_2 h^{-1} \| \mathbf{C}(\nabla \odot \boldsymbol{v}_h) \|^2_{0,K^+ \cup K^-}. \tag{3.22}$$

Proof. The proof of (3.22) is based on the fact that $\nabla \odot \boldsymbol{u}_h^s$ is constant and is similar to that in [20]. To show (3.21), we first let

$$\mathbf{C}(\boldsymbol{k} \odot \boldsymbol{v}_h^s) = \begin{pmatrix} w_{11}^s & w_{12}^s \\ w_{11}^s & w_{11}^s \end{pmatrix},$$

for any $s = \pm$. Then

$$\begin{aligned} \| \mathbf{C}(\boldsymbol{k} \odot \boldsymbol{v}_h^s) \|^2_{0,\Gamma_K} = & \sum_{i,j=1}^{2} \| w_{ij}^s \|^2_{0,\Gamma_K} \le C_3 \sum_{i,j=1}^{2} h^{-1} \| w_{ij}^s \|^2_{0,K^s} \\ = & C_3 h^{-1} \| \mathbf{C}(\boldsymbol{k} \odot \boldsymbol{v}_h) \|^2_{0,K^s}, \end{aligned} \tag{3.23}$$

where we have used the following inequality for w_{ij}^s

$$\| w_{i,j}^s \|^2_{0,\Gamma_K} \le C_3 h \| w_{i,j}^s \|^2_{0,K^s} \tag{3.24}$$

for $i, j = 1, 2$ and $s = \pm$. The proof of the inequality (3.24) is similar to that in [39, Lemma 3.1].

By the definition of the weighted averaging (3.11) and the fact $\kappa^{\pm} \leq 1$, we obtain that

$$\begin{aligned}\|\{\{\mathbf{C}(\nabla \odot \boldsymbol{v}_h)\boldsymbol{n}\}\|_{0,\Gamma_K}^2 &\leq 2\|\mathbf{C}(\nabla \odot \boldsymbol{v}_h^+)\|_{0,\Gamma_K}^2 + 2\|\mathbf{C}(\nabla \odot \boldsymbol{v}_h^-)\|_{0,\Gamma_K}^2 \\ &\leq 2C_3 h^{-1}\left(\|\mathbf{C}(\nabla \odot \boldsymbol{v}_h^+)\|_{0,K^+}^2 + \|\mathbf{C}(\nabla \odot \boldsymbol{v}_h^-)\|_{0,K^-}^2\right) \\ &= 2C_3 h^{-1}\|\mathbf{C}(\nabla \odot \boldsymbol{v}_h)\|_{0,K^+\cup K^-}^2,\end{aligned}$$

which completes the proof of (3.22) with $C_2 = 2C_3$. □

Next, we establish the following relationship between the strain and stress tensor

Lemma 3.3. *Let* $\mathbf{C}$ *be the fourth-order stiffness tensor defined in* (2.15) *and* A *be any symmetric second-order tensor. Then, the following inequality holds*

$$\mathbf{C}A : \mathbf{C}A \leq (4\mu + 2\lambda)\mathbf{C}A : A. \tag{3.25}$$

Proof. By the definition of fourth-order stiffness tensor (2.15), it follows that

$$\mathrm{tr}(\mathbf{C}A) = \mathrm{tr}(2\mu A + \lambda \mathrm{tr}(A)\mathbb{I}_2) = (2\mu + 2\lambda)\mathrm{tr}(A). \tag{3.26}$$

Notice that

$$\mathbf{C}A : A = (2\mu A + \lambda \mathrm{tr}(A)\mathbb{I}_2) : A = 2\mu A : A + \lambda \mathrm{tr}(A)^2 \geq \lambda \mathrm{tr}(A)^2, \tag{3.27}$$

where we have used the fact $A : A \geq 0$. Using (3.26) and (3.27), we can deduce that

$$\mathbf{C}A : \mathbf{C}A = 2\mu(\mathbf{C}A : A) + \lambda \mathrm{tr}(\mathbf{C}A)\mathrm{tr}(A) \leq (4\mu + 2\lambda)\mathbf{C}A : A. \quad \square \tag{3.28}$$

With the preparations, we are ready to show our main result.

Theorem 3.4. *Let* $\boldsymbol{k}$ *be a quasi-momentum in the reduced Brillouin zone. Suppose the stabilizing parameter* $\hat{\gamma}$ *is large enough. Then, there exist* $C_4, C_5 > 0$ *such that the following continuity and coercivity results hold*

$$a_h(\boldsymbol{u}_h, \boldsymbol{v}_h) \leq C_4 |\!|\!| \boldsymbol{v}_h |\!|\!| \, |\!|\!| \boldsymbol{u}_h |\!|\!|, \tag{3.29}$$

$$a_h(\boldsymbol{u}_h, \boldsymbol{u}_h) \geq C_5 |\!|\!| \boldsymbol{u}_h |\!|\!|^2. \tag{3.30}$$

Proof. The continuity (3.29) is a direct implication the definition of the sesquilinear form (3.13) and the Cauchy–Schwarz inequality. It remains to show the coercivity (3.30). Letting $\boldsymbol{v}_h = \boldsymbol{u}_h$ in (3.13) and applying Young's inequality with ϵ imply

$$\begin{aligned}a_h(\boldsymbol{u}_h, \boldsymbol{u}_h) &= \sum_{s=\pm}\int_{\Omega^s} \mathbf{C}(\nabla_{\boldsymbol{k}} \odot \boldsymbol{u}_h) : (\overline{\nabla_{\boldsymbol{k}} \odot \boldsymbol{u}_h})d\boldsymbol{x} + \frac{\gamma}{h}\int_{\Gamma} [\![\boldsymbol{u}_h]\!] \cdot [\![\overline{\boldsymbol{u}_h}]\!] ds \\ &\quad + 2\mathrm{Re}\int_{\Gamma} \{\{\mathbf{C}\,(\nabla_{\boldsymbol{k}} \odot \boldsymbol{u}_h)\,\boldsymbol{n}\}\} \cdot [\![\overline{\boldsymbol{u}_h}]\!] ds \\ &\geq \sum_{s=\pm} (\mathbf{C}(\nabla_{\boldsymbol{k}} \odot \boldsymbol{u}_h), \nabla_{\boldsymbol{k}} \odot \boldsymbol{u}_h)_{\Omega^s} + \frac{\gamma - 2\epsilon}{h}\|[\![\boldsymbol{u}_h]\!]\|_{0,\Gamma}^2 \\ &\quad - \frac{h}{\epsilon}\|\{\{\mathbf{C}\,(\nabla_{\boldsymbol{k}} \odot \boldsymbol{u}_h)\,\boldsymbol{n}\}\|_{0,\Gamma}^2 \\ &=: I_1 + I_2 - I_3.\end{aligned}$$

Notice I_1 and I_2 are already included in the mesh-dependent norm $|||\cdot|||$. We only need to estimate I_3. Let $\mu_m = \max(\mu^+, \mu^-)$ and $\lambda_m = \max(\lambda^+, \lambda^-)$. Using Lemmas 3.2 and 3.3, we deduce that

$$\begin{aligned}
I_3 =& \frac{h}{\epsilon}\|\{\{\mathbf{C}(\nabla_{\boldsymbol{k}} \odot \boldsymbol{u}_h)\boldsymbol{n}\}\}\|_{0,\Gamma}^2 \\
\leq& \frac{2h}{\epsilon}\|\{\{\mathbf{C}(\nabla \odot \boldsymbol{u}_h)\boldsymbol{n}\}\}\|_{0,\Gamma}^2 + \frac{2h}{\epsilon}\|\{\{\mathbf{C}(\boldsymbol{k} \odot \boldsymbol{u}_h)\boldsymbol{n}\}\}\|_{0,\Gamma}^2 \\
\leq& \frac{2C_1}{\epsilon}\|\mathbf{C}(\nabla \odot \boldsymbol{u}_h)\|_{0,\Omega^+\cup\Omega^-}^2 + \frac{2C_2}{\epsilon}\|\mathbf{C}(\boldsymbol{k} \odot \boldsymbol{u}_h)\|_{0,\Omega^+\cup\Omega^-}^2 \\
\leq& \frac{2C_1(4\mu_m + 2\lambda_m)}{\epsilon}\sum_{s=\pm}(\mathbf{C}(\nabla \odot \boldsymbol{u}_h), \nabla \odot \boldsymbol{u}_h)_{\Omega^s} + \\
& \frac{2C_2(4\mu_m + 2\lambda_m)}{\epsilon}\sum_{s=\pm}(\mathbf{C}(\boldsymbol{k} \odot \boldsymbol{u}_h), \boldsymbol{k} \odot \boldsymbol{u}_h)_{\Omega^s} \\
\leq& \frac{2C_4(4\mu_m + 2\lambda_m)}{\epsilon} I_1,
\end{aligned}$$

where we have used the Poincaré inequality (3.4) and $C_4 = \max(C_0C_1, C_0C_2)$.

Combining the above two estimates, we have

$$\begin{aligned}
& a_h(\boldsymbol{u}_h, \boldsymbol{u}_h) \\
\geq& (1 - \frac{2C_4(4\mu_m + 2\lambda_m)}{\epsilon})\sum_{s=\pm}(\mathbf{C}(\nabla_{\boldsymbol{k}} \odot \boldsymbol{u}_h), \nabla_{\boldsymbol{k}} \odot \boldsymbol{u}_h)_{\Omega^s} + \frac{\gamma - 2\epsilon}{h}\|[\![\boldsymbol{u}_h]\!]\|_{0,\Gamma}^2 \\
=& (1 - \frac{4C_4(4\mu_m + 2\lambda_m)}{\epsilon})\sum_{s=\pm}(\mathbf{C}(\nabla_{\boldsymbol{k}} \odot \boldsymbol{u}_h), \nabla_{\boldsymbol{k}} \odot \boldsymbol{u}_h)_{\Omega^s} + \\
& \frac{h}{\epsilon}\|\{\{\mathbf{C}(\nabla_{\boldsymbol{k}} \odot \boldsymbol{u}_h)\boldsymbol{n}\}\}\|_{0,\Gamma}^2 + \frac{\gamma - 2\epsilon}{h}\|[\![\boldsymbol{u}_h]\!]\|_{0,\Gamma}^2.
\end{aligned}$$

Taking $\epsilon = 8C_4(4\mu_m + 2\lambda_m)$ and $\hat{\gamma} \geq 4\epsilon\frac{\beta^+ + \beta^-}{\beta^+\beta^-}$, we conclude with proof of (3.30) with $C_5 = \min\{\frac{1}{2}, \frac{1}{\epsilon}\}$. □

From Theorem 3.4, we can see the discrete sesquilinear form (3.13) is continuous and coercive with respect to the mesh-dependent norm (3.20). The Lax–Milgram theorem implies the unfitted Nitsche's method (3.14) is well-posed. The spectral theory says the discrete eigenvalue of (3.14) can be listed as

$$0 < \omega_{h,1}^2 \leq \omega_{h,2}^2 \leq \cdots \leq \omega_{h,n_h}^2, \tag{3.31}$$

and the corresponding L^2 eigenfunctions are $\boldsymbol{u}_{h,1}, \boldsymbol{u}_{h,2}, \ldots, \boldsymbol{u}_{h,n_h}$ where n_h is the dimension of the Nitsche's finite element space $V_{h,per}$.

4. Error estimates

In this section, we shall conduct the error analysis for the proposed unfitted Nitsche's method (3.14) using the Babuška–Osborn theory. To this end, we introduce an extension operator X^s $(s = \pm)$ to extend an H^2 function defined on a subdomain Ω^s to the fundamental cell Ω. For a function $\boldsymbol{v} \in H^2(\Omega^s)$, the extend function $X^s\boldsymbol{v}$ is defined to satisfy

$$(X^s\boldsymbol{v})|_{\Omega^s} = \boldsymbol{v}, \tag{4.1}$$

and

$$\|X^s\boldsymbol{v}\|_{r,\Omega} \leq C\|\boldsymbol{v}\|_{r,\Omega^s}, \quad r = 0, 1, 2, \tag{4.2}$$

for $s = \pm$.

For $s = \pm$, let π_h^s be the Scott–Zhang interpolation operator [40] on $H^1(\Omega_h^s)$. The interpolation operator on the finite element space $V_{h,per}$ is defined as

$$I_h\boldsymbol{v} = (\pi_h^+X^+\boldsymbol{v}, \pi_h^-X^-\boldsymbol{v}) \in V_h. \tag{4.3}$$

Using the same argument as in [21], we can establish the following approximation property in the mesh-depending norm (3.20)

$$|||\boldsymbol{v} - I_h\boldsymbol{v}||| \lesssim h\|\boldsymbol{v}\|_{2,\Omega^+\cup\Omega^-}. \tag{4.4}$$

To adopt the Babuška–Osborn theory [27,28] , we define the solution operator $T : L^2(\Omega) \to H^1(\Omega^+ \cup \Omega^-)$ as

$$a_h(T\boldsymbol{f}, \boldsymbol{v}) = b(\boldsymbol{f}, \boldsymbol{v}), \quad \forall \boldsymbol{v} \in H^1(\Omega^+ \cup \Omega^-), \tag{4.5}$$

for any $\boldsymbol{f} \in L^2(\Omega)$. The interface eigenvalue problem (3.1) can be reinterpreted as

$$T\boldsymbol{u} = \zeta\boldsymbol{u}, \tag{4.6}$$

where $\zeta^{-1} = \omega^2$. Recall that we have excluded the exceptional case that $\omega^2 = 0$.

In a similar way, we can define the discrete solution operator $T_h : L^2(\Omega) \to V_{h,per}$ as

$$a_h(T_h\boldsymbol{f}, \boldsymbol{v}_h) = b(\boldsymbol{f}, \boldsymbol{v}_h), \quad \forall \boldsymbol{v} \in V_{h,per}, \tag{4.7}$$

for any $\boldsymbol{f} \in L^2(\Omega)$. Using the discrete solution operator, the discrete eigenvalue problem (3.14) is equivalent to

$$T_h\boldsymbol{u}_h = \zeta_h\boldsymbol{u}_h, \tag{4.8}$$

where $\zeta_h^{-1} = \omega_h^2$.

From the definition (3.13), the sesquilinear form $a_h(\cdot,\cdot)$ is Hermitian which implies both T and T_h are self-adjoint. It is also noted that T and T_h are compact operators from $L^2(\Omega)$ to $L^2(\Omega)$. For the solution operators T and T_h, we have the following estimates.

Theorem 4.1. *Let T be the solution operator defined in (4.5) and T_h be the discrete solution operator defined in (4.7). Then, we have*

$$|||T\boldsymbol{f} - T_h\boldsymbol{f}||| \le Ch\|\boldsymbol{f}\|_{0,\Omega}, \tag{4.9}$$

$$\|T\boldsymbol{f} - T_h\boldsymbol{f}\|_{0,\Omega} \le Ch^2\|\boldsymbol{f}\|_{0,\Omega}. \tag{4.10}$$

Proof. The error estimate (4.9) can be proved by combining orthogonality, continuity, and the coercivity of the sesquilinear form $a_h(\cdot,\cdot)$ and the approximation property of the interpolation operator (4.3). The error estimate (4.10) can be established using the Aubin–Nitsche's argument [30,31]. □

A direct consequence of Theorem 4.1 is

$$\|T - T_h\|_{\mathcal{L}(L^2(\Omega))} \le Ch^2. \tag{4.11}$$

Denote the resolvent set of the operator T (or T_h) by $\sigma(T)$ (or $\sigma(T_h)$) and the spectrum set of the operator T (or T_h) by $\rho(T)$ (or $\rho(T_h)$). Suppose ζ is an eigenvalue of the compact operator T with algebraic multiplicities m. Let $\mathcal{C}$ be a circle in the complex plane centered at ζ which is contained in resolvent set of T and encloses no other spectrum points of T. When h is sufficiently small, $\mathcal{C}$ is also contained in the resolvent set of T_h. We define the Riesz spectral projection associated with T and $\mathcal{C}$ as

$$E = \frac{1}{2\pi\mathrm{i}}\int_{\mathcal{C}}(z - T)^{-1}dz. \tag{4.12}$$

and the discrete analogue as

$$E_h = \frac{1}{2\pi\mathrm{i}}\int_{\mathcal{C}}(z - T_h)^{-1}dz. \tag{4.13}$$

According to [28], E is a projection onto the space of generalized eigenvectors associated with ζ and T.

Applying Babuška–Osborn theory [27,28] we have

Theorem 4.2. *Let ζ be an eigenvalue of T with algebraically multiplicity m and $\mathcal{C}$ be the circle defined above. Then, for sufficiently small h, the following statements hold.*

1. *There are exactly m eigenvalues $\zeta_{h,1}, \ldots \zeta_{h,m}$ of T enclosed in $\mathcal{C}$. Furthermore, $\lim_{h\to 0}\zeta_{h,j} = \zeta$, for all $j = 1, \ldots, m$.*

2. *E_h is an onto projection to the direct sum of the spaces of eigenvectors corresponding to these eigenvalues $\zeta_{h,1}, \dots \zeta_{h,m}$ of T.*
3. *There is a constant C independent of h such that*

$$\hat{\delta}(R(E), R(E_h)) \leq C\|(T - T_h)|_{R(E_h)}\|, \tag{4.14}$$

where $R(E)$ (or $R(E_h)$) is the range of the projection E (or E_h), $\hat{\delta}(R(E), R(E_h))$ stands for the gap between them, and $(T - T_h)|_{R(E_h)}$ is the restriction of $T - T_h$ to $R(E_h)$.

Now, we are in the position to present our main results on the numerical approximation of the eigenvalues and eigenfunctions:

Theorem 4.3. *Let ζ_h be an eigenvalue of T_h satisfying $\lim_{h\to 0} \zeta_h = \zeta$. Let $\boldsymbol{u}_h$ be a unit eigenvector of T_h corresponding to the eigenvalue ζ_h. Then there exists a unit eigenvector $\boldsymbol{u} \in R(E)$ such that the following estimates hold*

$$\|\boldsymbol{u} - \boldsymbol{u}_h\|_{0,\Omega} \leq Ch^2\|\boldsymbol{u}\|_{2,\Omega^+\cup\Omega^-}, \tag{4.15}$$

$$|\zeta - \zeta_h| \leq Ch^2\|\boldsymbol{u}\|_{2,\Omega^+\cup\Omega^-}, \tag{4.16}$$

$$|\omega^2 - \omega_h^2| \leq Ch^2\|\boldsymbol{u}\|_{2,\Omega^+\cup\Omega^-}. \tag{4.17}$$

Proof. First, we consider the approximation capability in the eigenfunction. To do this, we apply the approximation theory of abstract compact operator in [28]. Theorem 7.4 in [27] implies that

$$\|\boldsymbol{u} - \boldsymbol{u}_h\|_{0,\Omega} \leq \|(T - T_h)|_{R(E)}\|_{0,\Omega} = \sup_{\substack{\boldsymbol{v}\in R(E)\\ \|\boldsymbol{v}\|_h=1}} \|T\boldsymbol{v} - T_h\boldsymbol{v}\|_{0,\Omega} \leq Ch^2\|\boldsymbol{u}\|_{2,\Omega^+\cup\Omega^-},$$

where we have used the approximation property (4.11). This completes the proof of (4.15).

We then turn to the estimate (4.16). Without loss of generality, suppose $\boldsymbol{u}_1, \dots, \boldsymbol{u}_m$ form a basis for $R(E)$. Again, the Theorem 7.3 in [28] implies that there exists a constant C such that

$$|\zeta - \zeta_h| \leq C \sum_{j,k=1}^{m} |((T - T_h)\boldsymbol{u}_j, \boldsymbol{u}_k)| + C\|(T - T_h)|_{R(E)}\|_{0,\Omega}^2. \tag{4.18}$$

From (4.11), the second term in (4.18) is bounded above by $\mathcal{O}(h^2)$. We only need to estimate the first term in (4.18). By (4.5), (4.7) and the Galerkin orthogonality (3.19), we obtain that

$$\begin{aligned}
((T - T_h)\boldsymbol{u}_j, \boldsymbol{u}_k) =& (\boldsymbol{u}_j, (T - T_h)\boldsymbol{u}_k)\\
=& a_h(T\boldsymbol{u}_j, T\boldsymbol{u}_k - T_h\boldsymbol{u}_k)\\
=& a_h(T\boldsymbol{u}_j - T_h\boldsymbol{u}_j, T\boldsymbol{u}_k - T_h\boldsymbol{u}_k) + a_h(T_h\boldsymbol{u}_j, T\boldsymbol{u}_k - T_h\boldsymbol{u}_k)\\
=& a_h(T\boldsymbol{u}_j - T_h\boldsymbol{u}_j, T\boldsymbol{u}_k - T_h\boldsymbol{u}_k) + \overline{a_h(T\boldsymbol{u}_k - T_h\boldsymbol{u}_k, T_h\boldsymbol{u}_j)}\\
=& a_h(T\boldsymbol{u}_j - T_h\boldsymbol{u}_j, T\boldsymbol{u}_k - T_h\boldsymbol{u}_k)\\
\leq& C|||T\boldsymbol{u}_j - T_h\boldsymbol{u}_j|||\,|||T\boldsymbol{u}_k - T_h\boldsymbol{u}_k|||\\
\leq& Ch^2\|\boldsymbol{u}_j\|_{2,\Omega^+\cup\Omega^-}\|\boldsymbol{u}_k\|_{2,\Omega^+\cup\Omega^-}\\
\leq& Ch^2\|\boldsymbol{u}\|_{2,\Omega^+\cup\Omega^-}^2.
\end{aligned} \tag{4.19}$$

Combining the above two estimates gives the optimal approximation property of the eigenvalue (4.16). Apparently, the last estimate (3.31) follows immediately from (4.16) by noticing that $\zeta^{-1} = \omega^2$. □

5. Numerical examples

In this section, we shall use several benchmark numerical examples to validate our theoretical results and to illustrate the efficiency of the proposed unfitted numerical method in the computation of band structures of phononic crystals. In the following tests, we shall consider the aurum/epoxy phononic crystal and the aluminium/epoxy

Table 1
Material constants of aurum/aluminium/epoxy.

Parameters	Aurum (Ω^-)	Aluminium (Ω^-)	Epoxy (Ω^+)
Density ρ (kg/m^3)	19 500	2730	1180
Lame's constant λ (N/m^2)	4.23×10^{10}	4.59×10^{10}	4.23×10^{9}
Shear modulus μ (N/m^2)	2.99×10^{10}	2.70×10^{10}	1.57×10^{9}

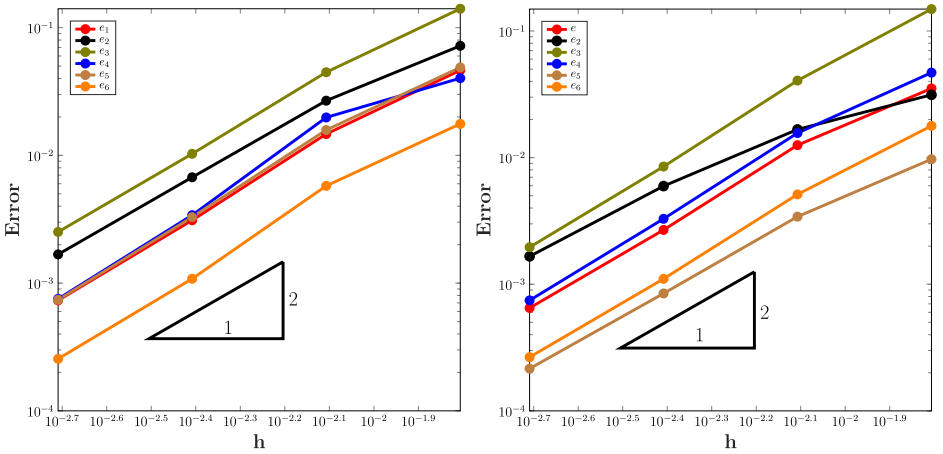

Fig. 3. Convergence rate of phononic crystal with circular inclusion. (a) aurum/epoxy phononic crystal; (b) aluminium/epoxy phononic crystal.

phononic crystal as in [18]. The aurum (Au) scatters or the aluminium (Al) scatters are embedded in the epoxy matrix. Their material constants are documented in Table 1. The transverse wave speed c^s is defined as

$$c^s = \sqrt{\mu^s/\rho^s} \tag{5.1}$$

for $s = \pm$. In all the following tests, the length of unit cell a is taken as 1.

To check the convergence rate for the unfitted Nitsche's method (3.14), we shall approximate the convergence rate of the exact error by the rate of the following the relative errors

$$e_i = \frac{\left|\omega^2_{i,h_j} - \omega^2_{i,h_{j+1}}\right|}{\omega^2_{i,h_j}},$$

where h_j is the mesh size of the jth level mesh and ω^2_{i,h_j} is the ith eigenvalue on the jth level mesh.

5.1. Square lattice with circular inclusion

In the first numerical example, we consider the square lattice with circular inclusion as shown in Fig. 1. As mentioned at the beginning of this section, the inclusion scatter is either aurum or aluminium and the material constants are listed in Table 1. The radius of the circular material interface is 0.25.

Firstly, we test the convergence for unfitted Nitsche's method (3.14). We take the quasi-momentum $\boldsymbol{k} = (\pi, \pi)$. The convergence history of the relative numerical errors is plotted in Fig. 3. As shown in Fig. 3, it is evident that the relative errors decay quadratically for both types of phononic crystals. The second-order convergence numerical results consist with the theoretical convergence rate predicted by Theorem 4.3. Note the jump ratios of the material parameters are about 19 for the aurum/epoxy phononic crystal and about 17 for the alumina/epoxy phononic crystal. Despite the high contrast and heterogeneous nature of the materials, the proposed numerical method is theoretically

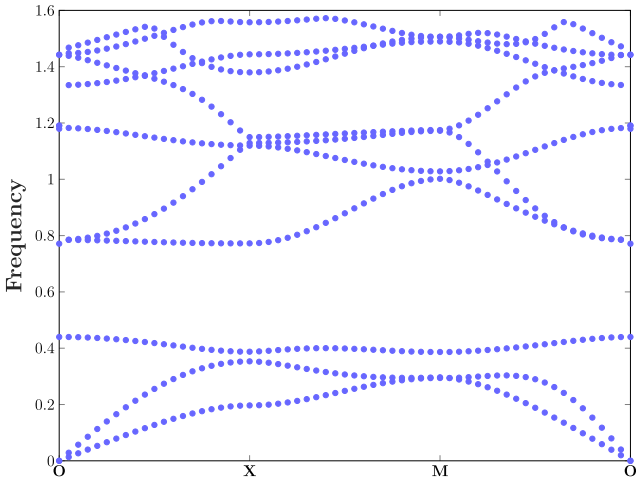

Fig. 4. Band structure of aurum/epoxy phononic crystal with circular inclusion.

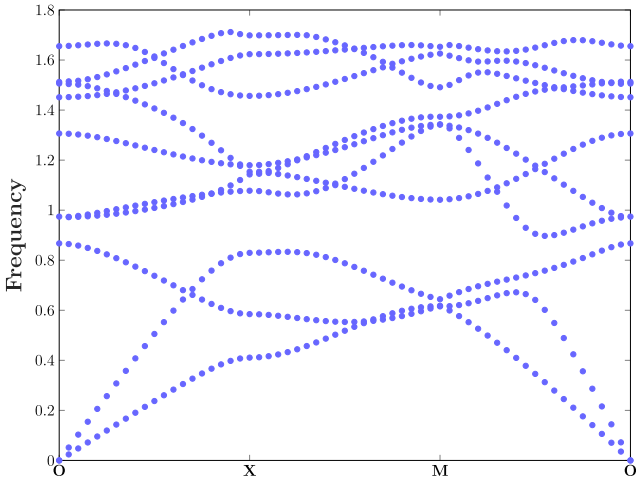

Fig. 5. Band structure of aluminum/epoxy phononic crystal with circular inclusion.

and numerically proven to achieve the optimal convergence rate, which demonstrates its capability in the efficient computation of band structures.

Now, we turn to the numerical computation of the band structure for the aurum/epoxy phononic crystal. In the computation, the mesh size is chosen to be $1/64$ and the quasi-momentum $\boldsymbol{k}$ is taken on the boundary of the irreducible Brillouin zone. In Fig. 4, we plot the first ten normalized frequency along the direction O–X–M–O. The normalized frequency is defined as $\omega a/(2\pi c^-)$ where c^- is the wave speed of the scatters defined in (5.1). From the graph, we can see that one small band-gap opens between the second eigencurve and the third eigencurve and one relatively large band-gap opens between the third eigencurve and the fourth eigencurve.

To compute the band structure of alumina/epoxy phononic crystal, we just replace aurum inclusions by alumina inclusions with the same size and shape. The first ten normalized eigenvalues are presented in Fig. 5. We see that the band structures changes dramatically. The original small gap which appears in the band structure of the aurum/epoxy crystal closes up in the alumina/epoxy crystal. And the bigger gap shrinks to a relatively small size.

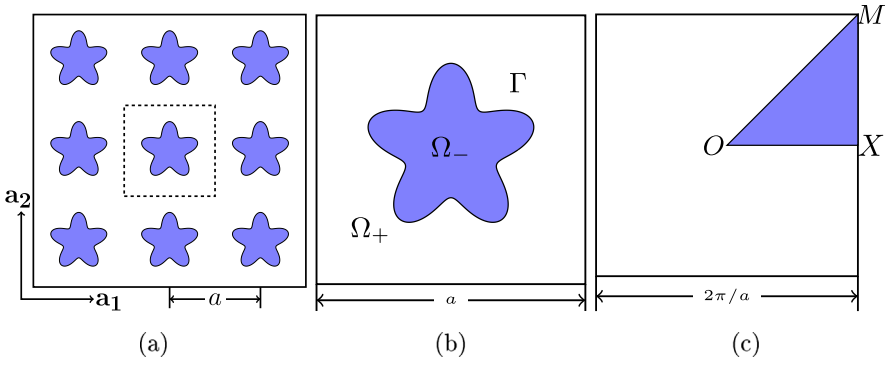

Fig. 6. Bravais lattice with flower shape inclusion. (a) 2D square lattice; (b) the unit cell; (c) the first Brillouin zone.

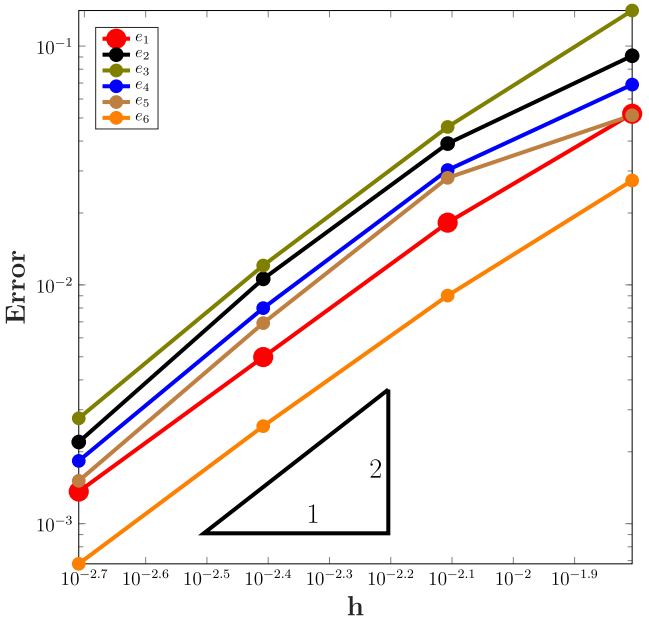

Fig. 7. Convergence rate of aurum/epoxy phononic crystal with flower shape inclusion.

5.2. *Square lattice with flower shape inclusion*

Our second numerical example is to handle aurum/epoxy phononic crystal with periodic flower shape inclusions. The phononic crystal is illustrated in Fig. 6. The flower material interface curve in polar coordinate is given by

$$r = \frac{1}{2} + \frac{\sin(5\theta)}{7}, \tag{5.2}$$

which contains both convex and concave parts. We conduct the computation in the fundamental cell Ω with length $a = 1$, see Fig. 6b.

As before, Fig. 7 shows the convergence curve of the relative error for the first six eigenvalues. What stands out in the figure is that the relative error converges optimally at the rate of $\mathcal{O}(h^2)$ as predicted by Theorem 4.2. The numerical results demonstrate the flexibility of the proposed method in handling interfaces with complicate geometries.

The band structure is also computed in this setup. In the test, we take the mesh size $h = \frac{1}{64}$. The first ten normalized frequency along O–M–X–O is plotted in Fig. 8. Similar to the aurum/epoxy phononic crystal with circular inclusions, here are two band-gaps: the relatively smaller band-gap is between the second and the third

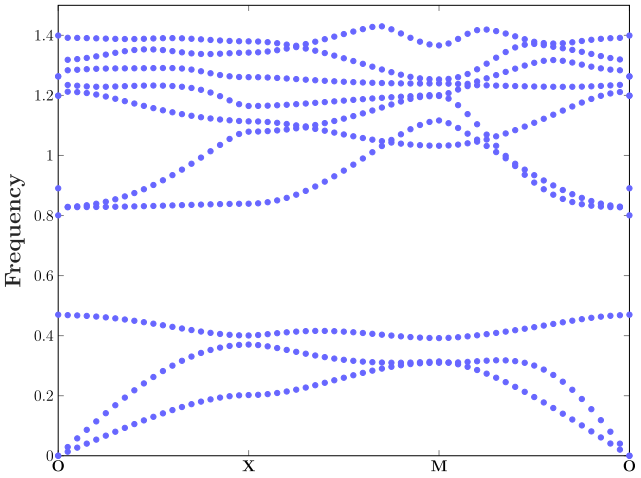

Fig. 8. Band structure of aurum/epoxy phononic crystal with flower shape inclusion.

eigencurves; the relative larger band-gap is between the third and the fourth eigencurves. An inspection of the data in Fig. 8 reveals that the band-gap is relatively larger than the circular inclusion case.

6. Conclusions

In this paper, a new finite element method for computing band structures of phononic crystals with general material interfaces is proposed. To handle the quasi-periodic boundary condition, we transform the equation into an equivalent interface eigenvalue problem with periodic boundary conditions by applying the Floquet–Bloch transform. The distinguishing feature of the proposed method is that it does not require the background mesh to fit the material interface which avoids the heavy burden of generating a body-fitted mesh and simplifies the impose of periodic boundary condition. Furthermore, the performance of the proposed method is theoretically founded. We show the well-posedness of the proposed method by using a delicate argument of the trace inequality. With the aid of the Babuška–Osborn theory, we prove the proposed method achieves the optimal convergence result at the presence of material interfaces. The theoretical convergence rate is validated by two realistic numerical examples, one of which involves a material interface with a complicated geometry. Thus our method is capable to compute band structures of very generic photonic crystals.

Declaration of competing interest

The authors declare that they have no known competing financial interests or personal relationships that could have appeared to influence the work reported in this paper.

Acknowledgments

H.G. was partially supported by Andrew Sisson Fund of the University of Melbourne, Australia, X.Y. was partially supported by the National Science Foundation, USA under grant DMS-1818592, and Y.Z. was partially supported by National Natural Science Foundation of China under grant 11871299.

References

[1] E.N. Economou, M. Sigalas, Stop bands for elastic waves in periodic composite materials, J. Acoust. Soc. Am. 95 (1994) 1734–1740.
[2] H. Ammari, H. Kang, H. Lee, Asymptotic analysis of high-contrast phononic crystals and a criterion for the band-gap opening, Arch. Ration. Mech. Anal. 193 (2009) 679–714.
[3] O. Sigmund, J. Jensen, Systematic design of phononic band–gap materials and structures by topology optimization, Phil. Trans. R. Soc. A 361 (2003) 1001–1019.
[4] Y. Liu, X. Chen, Y. Xu, Topological phononics: From fundamental models to real materials, Adv. Funct. Mater. 30 (2020) 1904784.
[5] M.S. Kushwaha, P. Halevi, L. Dobrzynski, B. Djafari-Rouhani, Acoustic band structure of periodic elastic composites, Phys. Rev. Lett. 71 (1993) 2022–2025.

[6] M.M. Sigalas, C.M. Soukoulis, Elastic-wave propagation through disordered and/or absorptive layered systems, Phys. Rev. B 51 (1995) 2780–2789.
[7] M. Kafesaki, E.N. Economou, Multiple-scattering theory for three-dimensional periodic acoustic composites, Phys. Rev. B 60 (1999) 11993–12001.
[8] Y. Cao, Z. Hou, Y. Liu, Finite difference time domain method for band-structure calculations of two-dimensional phononic crystals, Solid State Commun. 132 (2004) 539–543.
[9] H. Zheng, C. Zhang, Y. Wang, J. Sladek, V. Sladek, Band structure computation of in-plane elastic waves in 2D phononic crystals by a meshfree local RBF collocation method, Eng. Anal. Bound. Elem. 66 (2016) 77–90.
[10] F. Casadei, J. Rimoli, M. Ruzzene, Multiscale finite element analysis of wave propagation in periodic solids, Finite Elem. Anal. Des. 108 (2016) 81–95.
[11] R. Hu, C. Oskay, Spectral variational multiscale model for transient dynamics of phononic crystals and acoustic metamaterials, Comput. Methods Appl. Mech. Engrg. 359 (2020) 112761, 26.
[12] E. Li, Z.C. He, G. Wang, G.R. Liu, An ultra-accurate numerical method in the design of liquid phononic crystals with hard inclusion, Comput. Mech. 60 (2017) 983–996.
[13] I.A. Veres, T. Berer, O. Matsuda, Complex band structures of two dimensional phononic crystals: Analysis by the finite element method, J. Appl. Phys. 114 (2013) 083519.
[14] C. Comi, J.-J. Marigo, Homogenization approach and Bloch-Floquet theory for band-gap prediction in 2D locally resonant metamaterials, J. Elasticity 139 (2020) 61–90.
[15] H. Ammari, H. Lee, H. Zhang, Bloch waves in bubbly crystal near the first band gap: a high-frequency homogenization approach, SIAM J. Math. Anal. 51 (2019) 45–59.
[16] H. Ammari, B. Fitzpatrick, H. Kang, M. Ruiz, S. Yu, H. Zhang, Mathematical and Computational Methods in Photonics and Phononics, in: Mathematical Surveys and Monographs, vol. 235, American Mathematical Society, Providence, RI, 2018.
[17] W. Li, W. Chen, Simulation of the band structure for scalar waves in 2D phononic crystals by the singular boundary method, Eng. Anal. Bound. Elem. 101 (2019) 17–26.
[18] L. Wang, H. Zheng, X. Lu, L. Shi, A Petrov-Galerkin finite element interface method for interface problems with Bloch-periodic boundary conditions and its application in phononic crystals, J. Comput. Phys. 393 (2019) 117–138.
[19] A. Hansbo, P. Hansbo, An unfitted finite element method, based on Nitsche's method, for elliptic interface problems, Comput. Methods Appl. Mech. Engrg. 191 (2002) 5537–5552.
[20] A. Hansbo, P. Hansbo, A finite element method for the simulation of strong and weak discontinuities in solid mechanics, Comput. Methods Appl. Mech. Engrg. 193 (2004) 3523–3540.
[21] P. Hansbo, M.G. Larson, K. Larsson, Cut finite element methods for linear elasticity problems, in: Geometrically Unfitted Finite Element Methods and Applications, in: Lect. Notes Comput. Sci. Eng., vol. 121, Springer, Cham, 2017, pp. 25–63.
[22] E. Burman, S. Claus, P. Hansbo, M.G. Larson, A. Massing, CutFEM: discretizing geometry and partial differential equations, Internat. J. Numer. Methods Engrg. 104 (2015) 472–501.
[23] H. Guo, X. Yang, Gradient recovery for elliptic interface problem: III. Nitsche's method, J. Comput. Phys. 356 (2018) 46–63.
[24] H. Guo, X. Yang, Y. Zhu, Unfitted Nitsche's method for computing wave modes in topological materials, 2019, arXiv e-prints, arXiv :1908.06585, https://arxiv.org/abs/1908.06585.
[25] C. Valencia, J. Gomez, N. Guarín-Zapata, A general-purpose element-based approach to compute dispersion relations in periodic materials with existing finite element codes, J. Theor. Comput. Acoust. 27 (2019) 1950005.
[26] S.C. Aduloju, T.J. Truster, A primal formulation for imposing periodic boundary conditions on conforming and nonconforming meshes, Comput. Methods Appl. Mech. Engrg. 359 (2020) 112663, 29.
[27] I. Babuška, J.E. Osborn, Finite element-Galerkin approximation of the eigenvalues and eigenvectors of selfadjoint problems, Math. Comp. 52 (1989) 275–297.
[28] I. Babuška, J.E. Osborn, Eigenvalue problems, in: Handbook of Numerical Analysis, Vol. II, Handb. Numer. Anal. II, Amsterdam, 1991, pp. 641–787.
[29] C. Kittel, Introduction to Solid State Physics, 8th ed., John Wiley & Sons, Inc., New York, 2004.
[30] S.C. Brenner, L.R. Scott, The Mathematical Theory of Finite Element Methods, third ed., in: Texts in Applied Mathematics, vol. 15, Springer, New York, 2008.
[31] P.G. Ciarlet, The Finite Element Method for Elliptic Problems, in: Classics in Applied Mathematics, vol. 40, Society for Industrial and Applied Mathematics (SIAM), Philadelphia, PA, 2002, Reprint of the 1978 original [North-Holland, Amsterdam; MR0520174 (58 #25001)].
[32] L.C. Evans, Partial Differential Equations, second ed., in: Graduate Studies in Mathematics, vol. 19, American Mathematical Society, Providence, RI, 2010.
[33] J.P. Lee-Thorp, M.I. Weinstein, Y. Zhu, Elliptic operators with honeycomb symmetry: Dirac points, edge states and applications to photonic graphene, Arch. Ration. Mech. Anal. 232 (2019) 1–63.
[34] P. Xie, Y. Zhu, Wave packet dynamics in slowly modulated photonic graphene, J. Differential Equations 267 (2019) 5775–5808.
[35] S. Sticko, G. Ludvigsson, G. Kreiss, High-order cut finite elements for the elastic wave equation, Adv. Comput. Math. 46 (2020) 45.
[36] E. Burman, Ghost penalty, C. R. Math. Acad. Sci. Paris 348 (2010) 1217–1220.
[37] B. Müller, F. Kummer, M. Oberlack, Highly accurate surface and volume integration on implicit domains by means of moment-fitting, Internat. J. Numer. Methods Engrg. 96 (2013) 512–528.
[38] M. Juntunen, R. Stenberg, Nitsche's method for general boundary conditions, Math. Comp. 78 (2009) 1353–1374.
[39] H. Wu, Y. Xiao, An unfitted hp-interface penalty finite element method for elliptic interface problems, J. Comput. Math. 37 (2019) 316–339.
[40] L.R. Scott, S. Zhang, Finite element interpolation of nonsmooth functions satisfying boundary conditions, Math. Comp. 54 (1990) 483–493.